Electronic Supplementary Material (ESI) for Materials Horizons.

Electronic Supplementary Information:

Experimental Methods
Figures S1-S8
SPhP dispersion in a chain of nanoparticles
Thermal conduction by waves propagating along nanoparticle chains
Thermal conduction by many-body radiation

Experimental Methods

Amorphous SiO_2 and polycrystalline Si nanoparticles were purchased from US Research Nanomaterials, Inc. and Sigma-Aldrich. Fourier-transform infrared (FTIR) attenuated transmission reflection (ATR) spectroscopy was performed on the as-received nanoparticles using a Perkin Elmer Spectrum 100 FTIR spectrometer with a Pike VeeMax II variable angle ATR attachment. Zinc selenide (index of refraction = 2.4) was chosen for the ATR crystal (the nanoparticles were compressed into films on this substrate). For frequencies greater 207 Trad s^{-1}, the refractive index for SiO_2 never exceeds 1.5, so the critical angle is 38.7° (or less). For frequencies less than 207 Trad s^{-1}, the refractive index of SiO_2 exceeds that of zinc selenide and has a large imaginary part resulting in high external reflection by the bulk SiO_2 even in the lower frequency range. Furthermore, diffuse reflectance results are also present in the nanoparticle bed spectra. Thus the FTIR-ATR spectra are combined ATR, external reflectance, and diffuse reflectance results.

Thermal conductivity, thermal diffusivity, and volumetric specific heat of packed nanoparticle beds were measured between -50 and 200 °C with the Hot Disk TPS 2500 S transient plane source thermal constants analyser following international standard ISO 22007-2. This standard has an established thermal conductivity measurement uncertainty range of 2-5%. The transient nature of the technique, combined with the transient plane source model used in the Hot Disk TPS 2500 S, allows thermal conductivity, thermal diffusivity, and specific heat to be measured independently. The measurement uncertainty range is 5-10% for thermal diffusivity and specific heat. Our measurements were carefully calibrated on materials with known properties, and made at least 3 times for each collected data point to minimize uncertainty. Nanoparticles were packed on both sides of a Kapton measurement sensor into a stainless steel cylindrical holder with about 2 kPa. The nanoparticles were added to the holder in steps so that the 2 kPa weight could be used to compress the nanoparticles in increments to ensure even packing on both sides of the sensor. We do not expect that the nanoparticles are packed into perfect crystals, and we expect natural variations in packing geometry in reproduced experiments (Fig. S1), which indicates that our theoretical relation for surface phonon polariton crystals predicts trends even for less ordered nanoparticle arrangements.

For the adsorbed water system, The Hot Disk measurement sensor and sample holder containing the nanoparticles were placed in a Tenney Junior environmental test chamber to control the sample temperature. The samples were dried in the environmental chamber before each test by flowing dry air at 150 °C for at least 1 hour (except for the tests in Fig. S1B inset to compare), to establish an air interface at the nanoparticle surfaces. The airflow was stopped, and the chamber closed, to begin measurements. Each sample was measured for 3 consecutive temperature sweeps – from 150 to -50 °C, -50 to 150 °C, and 150 to -50 °C. The samples were held at each measurement set point for about 1 hour to reach steady state, and 30-60 min to collect data from several measurements. Using 3 temperature sweeps allowed adsorbed water to return in the second, increasing temperature sweep to increase the relative permittivity of the medium at the nanoparticle surface interface.

Relative humidity in the chamber was measured with an Omega HX15-W High-Temperature Relative Humidity/Temperature Transmitter, and humidity ratio was calculated from measured relative humidity, measured temperature, and ambient pressure. The humidity ratio uncertainties are maximum values for each given range calculated by propagation of uncertainty. The chamber humidity ratio was between 1% and 3% $\pm$ 0.3% during the second sweep – the amount of humidity was undetectable in the two decreasing temperature sweeps. The third temperature sweep was intended to reveal any hysteresis, and none was observed. The data collected at higher chamber humidity (up to 18.7% $\pm$ 2.7% humidity ratio) in Fig. 3B was obtained by placing a water-soaked sponge in the chamber during an increasing temperature test.

The ethylene glycol coated nanoparticles were prepared with a solution chemistry process. 4.8 g of as-received nanoparticles were mixed with 60 equivalents ethylene glycol (267 mL) or with 30 equivalents ethylene glycol (134 mL) and 100 equivalents deionized water (144 mL). Ethylene glycol was purchased from Sigma-Aldrich and McMaster-Carr. The solution was heated and stirred at 105-115 °C for 4 hours, cooled, and centrifuged at 25,000 rpm for 20 min to separate the coated nanoparticles. The resulting samples were baked in a dry environment at 115 °C for 4 hours to remove any remaining water. Thermal properties were measured with a similar method as the uncoated nanoparticles. Testing began at 0 °C or ambient temperature and proceeded in increasing temperature steps. Near the boiling point of ethylene glycol, thermal conductivity sharply decreased (Fig. 3C). Measurements at 200 °C are only reported for the datasets in which thermal conductivity had stabilized by the time of the measurement. When a stable measurement was obtained at 200 °C, an additional measurement was then taken at 190 °C to show the return to the phonon value of thermal conductivity of SiO_2 nanoparticle beds. The loss of ethylene glycol near the boiling point suggests that the nanoparticles were coated through hydrogen bonding interactions. Weight measurements before and after testing along with thermogravimetric analysis show the samples typically consisted of about 40% SiO_2 by weight. The differential scanning calorimetry measurement was performed with a TA Instruments Q2000 DSC.

Reproducibility of thermal conductivity measurements

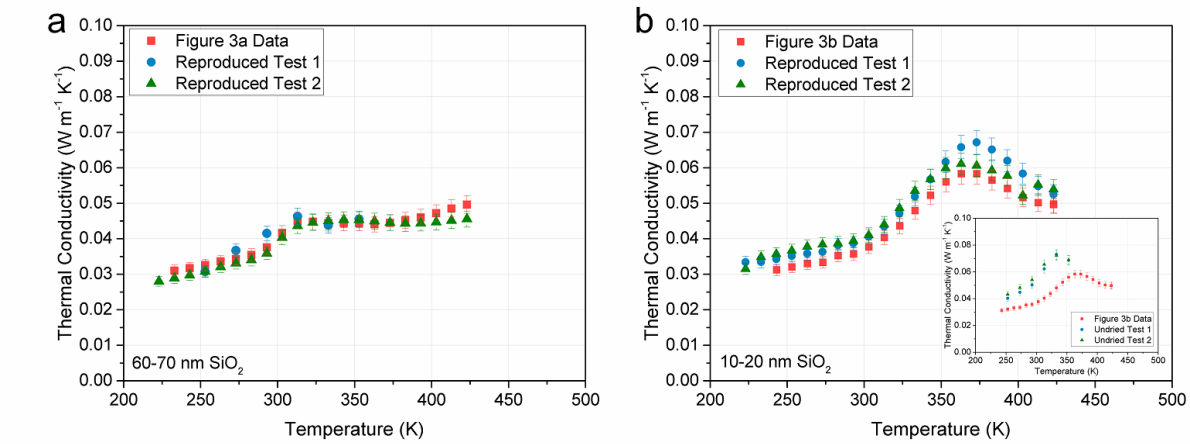

Fig. S1. (A) Thermal conductivity of SiO_2 nanoparticles 60-70 nm in diameter as a function of temperature. The SPhP red square data are from the main text Fig. 3A. The two reproduced experiments were conducted at different times, with fresh nanoparticles each time, over the span of one year. **(B)** Thermal conductivity of SiO_2 nanoparticles 10-20 nm in diameter as a function of temperature. The red square data are from the main text Fig. 3B. The two reproduced experiments were conducted at different times, with fresh nanoparticles each time, over the span of one year. The inset shows two reproduced experiments conducted prior to the measurements in Fig. 3B, both with fresh nanoparticles each time. The nanoparticles were not dried before the test to collect the data in the inset, which increased the content of adsorbed water similarly to the high humidity data in Fig. 3B. The error bars in all measurements are +/- 5% based on the uncertainty of the measurement technique, which is greater than the standard deviation of several measurements at each temperature.

Thermal conductivity of packed Si nanoparticle beds

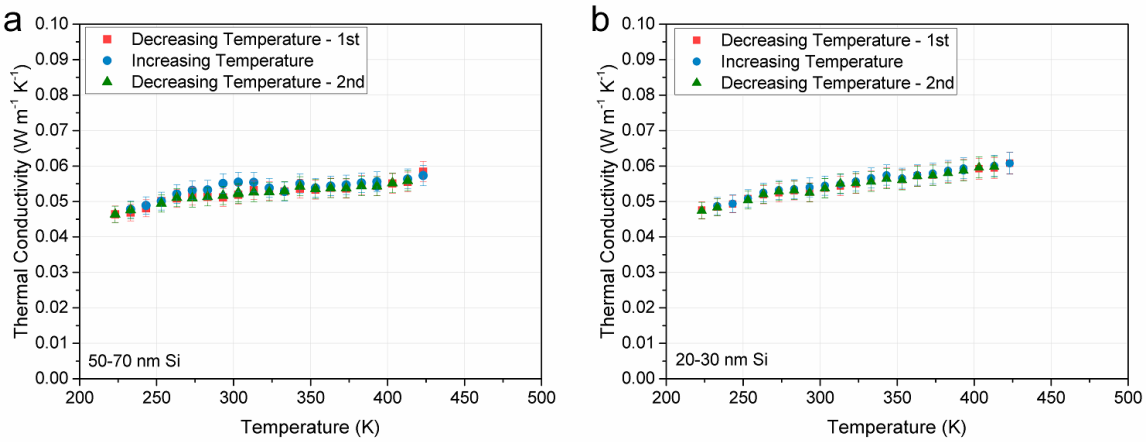

Fig. S2. (A) Thermal conductivity of Si nanoparticles 50-70 nm in diameter as a function of temperature. **(B)** Thermal conductivity of Si nanoparticles 20-30 nm in diameter as a function of temperature. The error bars in all measurements are +/- 5% based on the uncertainty of the measurement technique, which is greater than the standard deviation of several measurements at each temperature. The data for three consecutive temperature sweeps as described in the Experimental Methods section overlap within the experimental uncertainty for each data set. The lack of a departure from the linear trend in the temperature increase is evidence that adsorbed water does not play a role in heat transfer through the bed.

Specific heat of packed SiO_2 nanoparticle beds

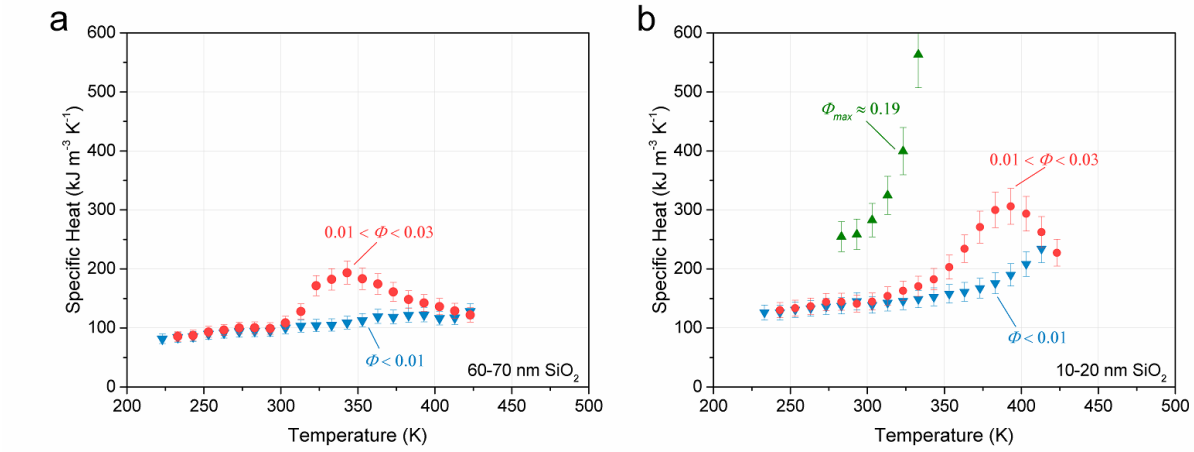

Fig. S3. (A) Measured specific heat of SiO_2 nanoparticles 60-70 nm diameter as a function of temperature. This is the same sample as shown in Fig. 3A in the main text. **(B)** Measured specific heat of SiO_2 nanoparticles 10-20 nm diameter as a function of temperature. This is the same sample as shown in Fig. 3B in the main text. The specific heat in **(A)** and **(B)**, with water adsorbed (the higher humidity ratio data sets), includes contributions from the SPhP specific heat, phonon specific heat, and adsorbed water. Similarities in shape to the thermal conductivity data in Figure 3 of the main text suggest that SPhPs may affect the specific heat, as well as possible contributions from the presence of adsorbed water and phase change. The peaks in specific heat are not at the same locations as the peaks in thermal conductivity, which illustrates the independence of the thermal conductivity and specific heat measurements. These trends have additionally been validated with Differential Scanning Calorimetry measurements. The data sets for each SiO_2 sample correspond to consecutive temperature sweeps as described in the Experimental Methods. The error bars in all measurements are +/- 10% based on the uncertainty of the measurement technique, which is greater than the standard deviation of several measurements at each temperature. The peaks in the temperature dependent specific heat correspond to the release of adsorbed molecular water layers.

Specific heat of packed Si nanoparticle beds

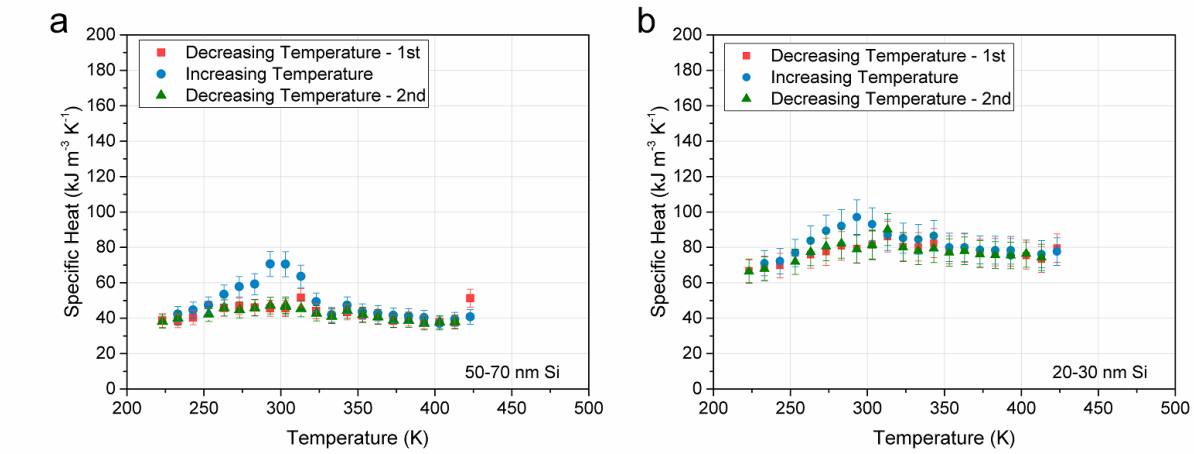

Fig. S4. (A) Measured specific heat of Si nanoparticles 50-70 nm diameter as a function of temperature. **(B)** Measured specific heat of Si nanoparticles 20-30 nm diameter as a function of temperature. The three data sets for each sample correspond to three consecutive temperature sweeps as described in the Experimental Methods. The error bars in all measurements are +/- 10% based on the uncertainty of the measurement technique, which is greater than the standard deviation of several measurements at each temperature. The magnitudes of these specific heat data are close to half the magnitudes of values for specific heat data for SiO_2, so the contribution of the specific heat of adsorbed water could be larger in this case. The peaks in specific heat are not accompanied by a peak in thermal conductivity (Fig. S2), which differs from the case for SiO_2. The peaks in specific heat are attributed to the transition from solid to liquid water, which increases the water specific heat by about two times,[1] and then the loss in water content from its incremental release at increased temperatures.

SPhP dispersion in a chain of nanoparticles

The equation for the SPhP dispersion relation for a chain of polar nanoparticles is given by Equation (3). This equation contains an infinite summation representing the number of nanoparticles to include in the dispersion, but in our calculations we use only the first five terms. To show that higher terms are negligible, we plot below the dispersion relation for N = 1 to N = 5 terms, which clearly shows convergence for N = 5.

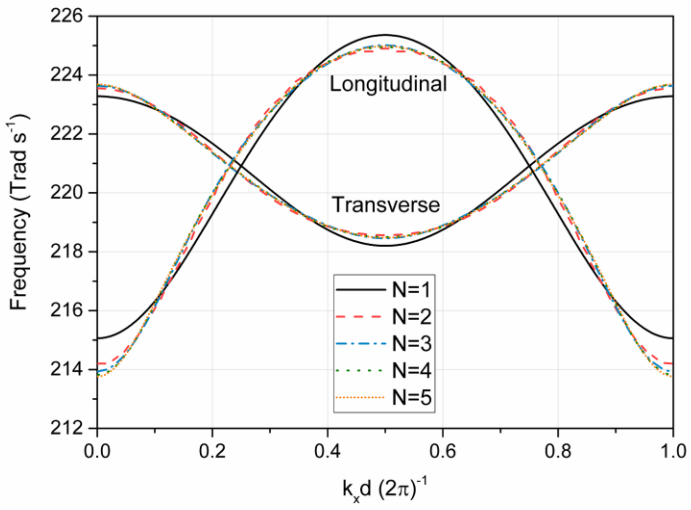

Fig. S5. The SPhP dispersion relation is plotted for a chain of 65 nm diameter particles in contact. We plot the dispersion for N = 1 to N = 5 nanoparticles, and the dispersion converges for N =5.

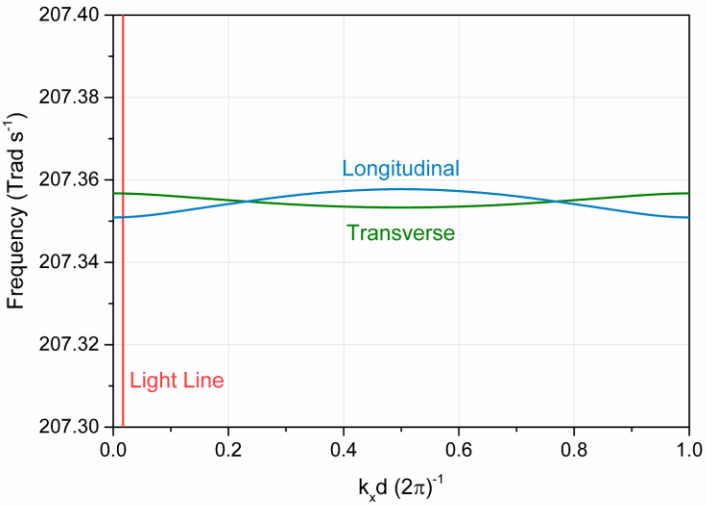

Fig. S6. The SPhP dispersion relation for SiO_2 particles in a water medium ($\varepsilon_m = 80$) is plotted along with the light line. The light line intersects both the transverse and longitudinal modes near 207 rad s^{-1}, which is used for comparison with our FTIR-ATR measurements (Fig. 2 inset).

Thermal conduction by waves propagating along nanoparticle chains

The slope of the dispersion curves shows that the wave coupling between nanoparticles can carry energy along the chain. This motivates the model of thermal conduction by SPhP wave propagation along nanoparticle chains, which has been theoretically investigated by other researchers.[2-4] The equation for one-dimensional diffusive thermal conductivity in this scenario developed by Ben-Abdallah et al.[3] with kinetic theory is:

$$\kappa = \frac{1}{\pi A}\frac{\hbar^2}{k_B T^2}\sum_p \int_0^{Br} v_g^2(k)\gamma(k)\omega^2(k)\frac{e^{\hbar\omega/k_B T}}{(e^{\hbar\omega/k_B T}-1)^2}\,dk \qquad \text{(S1)}$$

where $A,\ T, Br, v_g,$ and γ are the cross-sectional area of the chain, temperature, edge of the first Brillion zone $2\pi/d$, group velocity, and mode lifetime. The mode lifetime can be simply approximated as $\gamma = 2/\Gamma$,[5] where Γ is the damping constant (8.92 Trad s^{-1} for SiO_2). Together, the group velocity times the mode lifetime $v_g\gamma$ is the same as the propagation length[6] Λ (mean free path), which is related to the probability of transmission in the diffusive regime[7] by $\tau = \Lambda/\mathrm{L}$ where L is the length of the system. This leads to a strong dependence on the group velocities in the dispersion, which can be seen by the dispersion and calculated thermal conductivity curves in Fig. 5 & 6 in the main text. When the dispersion occupies a narrower frequency range (higher density of states) when the medium permittivity increases, the group velocities decrease, causing the thermal conductivity to drop (Fig. 6). Note that the thermal conductivity equation in three-dimensions (our system) will have the same dependence on group velocity and mode lifetime.[7] We also calculate the propagation lengths based on the group velocities in the dispersion relation (Fig. 5) by $\Lambda = v_g\gamma$ and plot the results below for a chain of 65 nm diameter SiO_2 particles in contact with a medium relative permittivity of $\varepsilon_m = 1$ and $\varepsilon_m = 4$. The results show that the propagation lengths are on the order of the nanoparticle spacing, which raises doubts about the applicability of a propagating wave model.

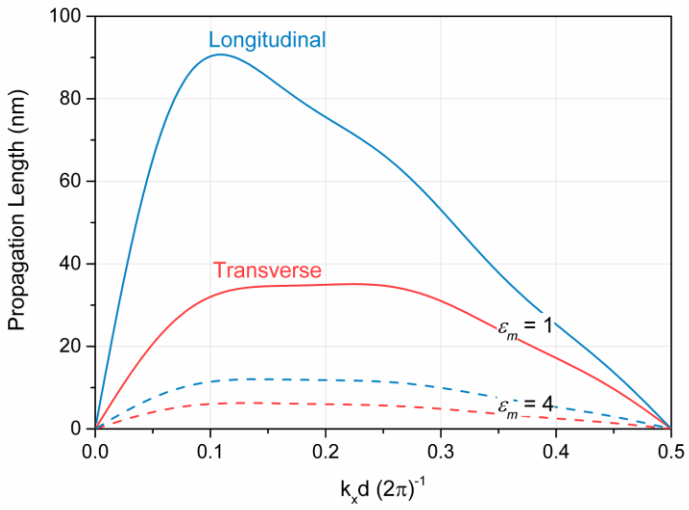

Fig. S7. Propagation length of SPhPs in a 65 nm diameter SiO_2 nanoparticle chain in contact based on our derived dispersion relationship. The blue lines are for longitudinal polarization and the red lines are for transverse polarization. The solid lines represent a medium relative permittivity of 1, and the dashed lines a medium relative permittivity of 4. The longest propagation lengths calculated are just longer than the inter-particle spacing.

Thermal conduction by many-body radiation

An alternative method of calculating thermal conductivity in a nanoparticle bed is through the coupled dipole method of many-body radiation.[8-11] The details of the model we implemented can be found in Ref. 8 and Ref. 10. In the second reference, Ben-Abdallah et al. calculate the thermal conductance between any two nanoparticles in a linear chain. To extend this method to find thermal conductivity, we first write an equation for the total heat flux along a chain of N nanoparticles with a temperature gradient along the chain axis dT/dx.

$$Q = \sum_{i=1}^{N-1} \sum_{j=i+1}^{N} G_{ij} \frac{dT}{dx} d(j-i) \tag{S2}$$

where G_{ij} is the thermal conductance between the ith and jth nanoparticles and d is the inter-particle spacing. Using Fourier's law, we can then simply write thermal conductivity with the following expression.

$$\kappa = \frac{d}{A} \sum_{i=1}^{N-1} \sum_{j=i+1}^{N} G_{ij} (j-i) \tag{S3}$$

This equation was used to find the thermal conductivity curves plotted in Fig. 6 in the main text. We used $N = 61$ nanoparticles for our calculations and found that the thermal conductivity had converged by this value.

An explanation for why this model predicts declining thermal conductivity with increasing medium permittivity can be found by examining the model's dependence on the nanoparticle polarizability. The thermal conductance between the ith and jth nanoparticles depends on a transmission coefficient, given by Ben-Abdallah et al. as [8]

$$\mathcal{T}_i, j(\omega) = \frac{4}{3} \frac{\omega^4}{c^4} \mathrm{Im}(\alpha_i) \mathrm{Im}(\alpha_j) \mathrm{Tr}\left[\mathbb{G}^{ij} \mathbb{G}^{ij\dagger}\right] \tag{S4}$$

where $\mathbb{G}^{ij}$ is the dyadic Green's function between the two nanoparticles. We can quickly see that when the imaginary part of the polarizability decreases, the transmission coefficient will also decrease. For SiO_2 nanoparticles in the frequency range of interest, we indeed find that the polarizability will decrease with increasing medium permittivity. This is shown graphically below.

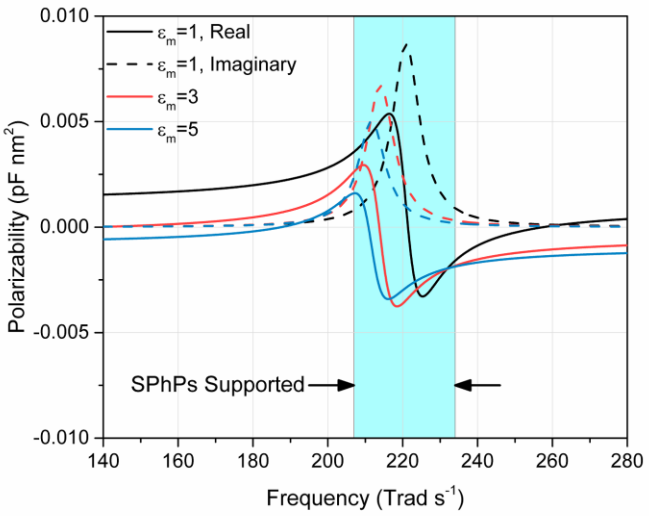

Fig. S8. Clausius-Mossotti polarizability of 65 nm diameter SiO_2 nanoparticles. The solid lines are the real part of the polarizability and the dashed lines are the imaginary part. Curves are given for values of medium relative permittivity of 1 (black), 3 (red), and 5 (blue). As the medium permittivity increases, the average imaginary permittivity also decreases, which leads to the drop in thermal conduction predicted by the many-body radiation model.

Author Contributions: B.A.C. and J.S.H. conceived and coordinated the work. O.S.A and J.S.H conducted spectroscopy measurements, and E.J.T., O.S.A. and J.S.H developed the dispersion relationship model. E.J.T. reviewed and implemented models taken from literature. E.J.T. and B.A.C. developed the thermal conductance and conductivity model and managed thermal conductivity measurements. E.J.T, B.A.C., and J.S.H wrote the paper.

Competing financial interests: The authors declare that they have no competing financial interests.

References

1. T. L. Bergman, F. P. Incropera, A. S. Lavine and D. P. DeWitt, *Fundamentals of heat and mass transfer*, John Wiley & Sons, seventh edn., 2011.

2. P. Ben-Abdallah, *Appl Phys Lett*, 2006, **89**, 113117.

3. P. Ben-Abdallah, K. Joulain, J. Drevillon and C. Le Goff, *Physical Review B*, 2008, **77**, 075417.

4. J. Ordonez-Miranda, L. Tranchant, S. Gluchko and S. Volz, *Physical Review B*, 2015, **92**, 115409.

5. D. Griffiths, *Introduction to electrodynamics*, Prentice hall Upper Saddle River, NJ, 1999.

6. G. Chen, *Nanoscale energy transport and conversion*, Oxford University Press, New York, 2005.

7. T. Fisher, *Thermal Energy at the Nanoscale*, World Scientific Publishing Co, 2014.

8. P. Ben-Abdallah, S.-A. Biehs and K. Joulain, *Physical Review Letters*, 2011, **107**, 114301.

9. A. D. Phan, T.-L. Phan and L. M. Woods, *Journal of Applied Physics*, 2013, **114**, 214306.

10. P. Ben-Abdallah, R. Messina, S.-A. Biehs, M. Tschikin, K. Joulain and C. Henkel, *Physical Review Letters*, 2013, **111**, 174301.

11. M. Nikbakht, *Journal of Applied Physics*, 2014, **116**, 094307.